Electro-Mechanical Properties of Graphene Drumheads

Nikolai N. Klimov[1-3], Suyong Jung[1,2,§], Shuze Zhu[4], Teng Li[2,4*], C. Alan Wright[4],

Santiago D.Solares[2,4*], David B. Newell[3], Nikolai B. Zhitenev[1], and Joseph A. Stroscio[1*]

[1]Center for Nanoscale Science and Technology, NIST, Gaithersburg, MD 20899

[2]Maryland NanoCenter, University of Maryland, College Park, MD 20742

[3]Physical Measurement Laboratory, NIST, Gaithersburg, MD 20899

[4]Department of Mechanical Engineering, University of Maryland, College Park, MD 20742

[§]Present address: Korea Research Institute of Standards and Science, Seoul, South Korea

Abstract:

The electro-mechanical properties of a suspended graphene layer were determined by scanning tunneling microscopy (STM) and spectroscopy (STS) measurements and computational simulations of the graphene membrane mechanics and morphology. A graphene membrane was continuously deformed by controlling the competing interactions with a STM probe tip and the electric field from a back gate electrode. The probe tip induced deformation created a localized strain field in the graphene lattice. STS measurements on the deformed suspended graphene display an electronic spectrum completely different from graphene supported by a substrate. The spectrum indicates the formation of a spatially confined quantum dot, in agreement with recent predictions of confinement by strain induced pseudomagnetic fields.

[*] To whom correspondence should be addressed: ssolares@umd.edu (S.D.S.); lit@umd.edu (T.L.); joseph.stroscio@nist.gov (J.A.S.)

Suspending graphene sheets can remove unwanted electrical potential disturbances from supporting substrates. Initial measurements of graphene devices on SiO_2 insulating substrates achieved carrier mobilities of ≈5000 $m^2\ V^{-1}\ s^{-1}$ *(1)*. Removing the substrate by suspending graphene resulted in mobilities in excess of 200,000 $m^2\ V^{-1}\ s^{-1}$ at low temperatures *(2)*. These differences illustrate how substrate-induced potential disorder due to impurities and strain can play a role in the electronic properties of graphene. Recently, strain engineering of electronic properties of graphene, which can be described through the generation of local pseudo scalar and magnetic fields by strain *(3–11)*, has attracted significant attention. For example, strain generated pseudomagnetic fields equivalent to a real magnetic field as high as 300 T have been reported *(5)*. However, a number of questions remain regarding the structure and electronic properties of suspended graphene layers.

In this report, we present scanning tunneling microscopy (STM) and scanning tunneling spectroscopy (STS) measurements of suspended graphene drumheads in a back-gated graphene device structure. We achieved stable STM measurements on the suspended graphene by carefully approaching the membrane with very slow scanning speeds. We observed that both the van der Waals forces from the STM probe tip and electrostatic force induced by back gate voltage can induce substantial mechanical deformation in the suspended graphene membranes. The visible membrane shape measured as a tip height can be continuously tuned from concave to convex by adjusting the electrostatic force. However, the induced strain in the graphene membrane mainly originates from the tip-membrane interaction, dramatically altering the electronic spectrum of graphene compared to the measurements of graphene directly supported by a substrate *(12, 13)*. In particular, we observed multiple quartet bands of peaks in the differential conductance spectra characteristic of charge confinement in a quantum dot.

Theoretical simulations of the membrane mechanics and experimental results confirm recent predictions of quantum dot confinement in pseudomagnetic fields generated by rotationally symmetric strain fields in graphene membranes *(6, 7)*.

Figures 1, A to C, show the geometry of our graphene device used in this study. An array of pits was fabricated in SiO_2/Si substrates, 1.1 μm in diameter and 100 nm in depth, by shallow plasma etching of SiO_2 (Fig. 1C). Graphene flakes were exfoliated onto the pre-patterned SiO_2/Si substrate via mechanical exfoliation of natural graphite and contacted using a Pd/Au electrode deposited via a stencil mask (Fig.1B). After fabrication, the STM probe tip was aligned onto the device in ultrahigh vacuum by using an external optical microscope prior to cooling the STM module in a custom STM system operating at 4 K *(14)*.

STM topographic images of single-layer supported and suspended graphene over an area of 20 nm by 20 nm are shown in Fig. 1, D and E, respectively. On small length scales, the graphene honeycomb lattice was clearly resolved on both supported and suspended graphene, with comparable corrugation amplitudes (Figs. 1, D and E, insets). On the 20 nm length scale, the peak-to-peak height corrugation on the suspended graphene was about four times larger than that of the supported graphene on the SiO_2 substrate over this scan area range (Fig. 1F). The larger height variation on the graphene membrane indicates deformation of the graphene sheet, which become larger with greater scan sizes (Fig. 2).

In order to obtain STM images of suspended graphene, as in Fig. 1E, we had to approach the suspended graphene area from the supported edge at very low scan speed to avoid exciting the graphene drumhead. If the drumhead was excited, the STM servo loop would go into oscillation with uncontrolled amplitude. However, when the scan speed was kept sufficiently

low, a large continuous deformation of the graphene membrane could be observed as the tip scanned the graphene suspended over the pits in the substrate (Figs. 2, A to D). This visible deformation could be continuously tuned to be either positive (outward from the surface, Figs. 2, A to C) or negative (inward to the surface, Fig. 2D) depending on the magnitude of the voltage, V_{GATE}, applied to the back gate electrode.

The graphene deformation in Figs. 2, A to D was caused by the STM probe tip pulling up on the membrane via the van der Waals and electrostatic forces and the back gate electrode pulling the membrane down via electrostatic force. In the progression of images from Figs. 2, A to D, the force from the back gate was incrementally increased as V_{GATE} was changed from 0 to 60 V, which progressively pulled the membrane downward. Between 50 and 60 V, the forces from the probe tip were balanced by the gate field, and finally at 60 V, the force from the back gate pulled the graphene into the underlying pit. In contrast, a tip-membrane potential difference in the range of ±1 V and the related electrostatic force produced only a small effect on the membrane shape, implying that the van der Waals force between the probe tip and graphene membrane is the dominant pull-up force. We also augmented our spectroscopic measurements with molecular dynamics simulations discussed below.

To study the electronic properties of the suspended graphene membranes we applied high-resolution gate mapping STS measurements in which individual dI/dV spectra are measured at a fixed spatial location as a function of both tunneling bias, V_B, and back gate voltages, V_{GATE} (Fig. 3) *(12, 15)*. The dI/dV spectra, proportional to the local density of states, were used to examine how the suspension of the graphene affects its electronic spectrum. The unique electronic spectrum of graphene in a uniform applied magnetic field, B, consists of a set of quantized Landau levels (LLs) *(16, 17)*. Gate mapping measurements made on the suspended

membrane at the same fixed location (Figs. 3, A to D) show a graphene electronic spectrum dramatically different from the measurements on supported graphene layers *(12, 13)*. The notable signatures of the spectra of supported graphene (see refs. *(12, 13)*) are the following: 1) In zero applied magnetic field, tunneling spectra show a minimum at the Dirac point with its distinct square-root dispersion as a function of density *(18)*, and 2) In applied magnetic fields, magnetically quantized LLs form a stair case pattern in the gate maps as the LLs are sequentially pinned at the Fermi level. Spectra are very different on the suspended membrane. In zero applied magnetic field the dI/dV gate map (Fig. 3A) showed a new series of states seen as lines with a small negative slope with increasing gate voltage (almost horizontal across the gate map). In addition, a series of broad bands with positive slopes were observed, as indicated with the blue arrows in Fig. 3A. These latter features with positive slopes became more resolved in an applied magnetic field, seen at B = 5 T (Fig. 3 B) and B = 8 T (Figs. C and D), resembling the spectral signatures of quantum dots (QD) *(12),19)*. (see supplemental data *(18)* for a comparison of the gate maps on supported and suspended graphene).

To further explore the analogy with QD physics, we examine the energy scales in the spectral maps of the suspended graphene. As an example, dI/dV spectra, that are parts of the gate maps in Fig. 3A and Fig. 3C, are shown in Fig. 3E and Fig. 3F, respectively. The peaks in Fig. 3E corresponding to the horizontal lines in the zero field gate map (Fig. 3A) showed a separation of approximately 30 mV for the first few states. In contrast, the peaks in Fig. 3F that form the positive slope bands were seen in groups of four with a spacing of ≈20 mV. This grouping is similar to the four-fold charging peaks in QDs observed in graphene *(12)* or carbon nanotubes *(19)*, and reflects the four-fold degeneracy of the dot levels caused by electron spin and valley quantum numbers. These dI/dV peaks are caused by an opening up of a transport channel at the

Fermi energy associated with a single-electron addition to the QD. The peaks appeared as tilted lines in the map because the QD energy levels are controlled by a linear combination of the gate voltage and tip bias.

In the following, we use this analogy to determine the energy scale and the size of the QD from the measured slopes and spacing of the charging lines. The vertical voltage bias axis is converted to the quantum dot energy spacing using the lever arm, $E = \alpha V_{\mathrm{B}}$, where $\alpha = C_{\mathrm{B}} / C_{\mathrm{T}} \approx 0.4$, C_{B} is the graphene layer to graphene QD capacitance, and C_{T} the total capacitance of the quantum dot. In Fig. 3G we plot the energy difference between the levels from the gate maps in Fig. 3C (red symbols) and Fig. 3D (blue symbols). The energy spacing of the individual levels indeed follows the classic energy spectrum of a quantum dot *(20)*, $e^2 / C_{\mathrm{T}} + \Delta E_{N+1}$, where e^2 / C_{T} is the charging energy of the four-fold degenerate levels of a graphene quantum dot (base line in Fig. 3G), and the additional energy, $\Delta E_{N+1} = E_{N+1} - E_N$, separating each band (spikes in Fig. 3G), corresponds to the energy needed to reach the next quantum dot level. Here, *e* is the electron charge. The charging energies, varying from (11.7±0.5) to (5.3±0.7) meV in Fig. 3G, correspond to quantum dots with diameters in a range from (34±2) to (53±5) nm *(21)*. This dot size is consistent with a simple estimate based on the number of electrons added to the dot for a given range of gate voltage. In the gate map (Fig. 3C) we see approximately 5 quartet bands over the gate voltage range of 40 V, corresponding to the addition of 20 electrons to the quantum dot. Using the gate capacitance of 5.85 nF cm^{-2} (100 nm vacuum plus 200 nm oxide) yields a rough estimate of the dot diameter of 42 nm.

The profile of the membrane as measured by the tip height cannot explain the formation of a QD. To understand the local and the global membrane deformation and the corresponding

strain induced in the immediate vicinity of the STM tip, we performed molecular dynamics simulations *(18)*. The calculations involved approaching the membrane with the tip at three different horizontal locations along a radial line across the membrane (2.5 nm and 5.2 nm from the edge, as well as in the center of the membrane) and then retracting the tip until a critical point was reached, where further retraction of the tip would result in loss of tip-membrane contact *(18)*. This critical point simulates the action of the STM servo that redraws the tip from the membrane to avoid contact while it maintains a vacuum tunneling gap. Additionally, a constant force of magnitude in the range 0 to 0.06 pN was applied to each carbon atom of the membrane to simulate the electrostatic force exerted by the gate electrode. The range of the back gate force was selected such that different levels of membrane deformation took place above and below the neutral position (fig. S9) *(18)*.

Figure 2E illustrates the atomistic model used, showing the tip at the critical height above the pulled-up membrane. In Fig. 2F the membrane shapes at the critical tip height are plotted together for three tip locations on a membrane, for a back gate force of 0.012 pN per atom. The computational simulations show that the deformation in the graphene membrane induced by the probe tip is formed locally. The simulations further demonstrate that the measured membrane profiles are not caused by a static membrane deformation, but one that continuously changes with the tip position. As the STM tip is rastered across a membrane, the cusp of the deformation follows the tip (Fig. 2F), and the dome-like shapes recorded in STM images (Figs. 2, A to D) are the envelopes tracing the cusp peak as illustrated by the dashed line in Fig. 2F.

The mechanical simulations also show that the deformation in the graphene lattice induced a strain in the membrane (Fig. 4A), which was localized on the small scale of the probe tip diameter (5 nm) used in the simulation. A scaling analysis (figs. S12, S13) *(18)* shows the

deformation area scales with the square root of the probe tip diameter for a flat membrane. Extrapolating the deformation size for the experimental probe diameter of 100 nm (determined by SEM) yields a strain field diameter of approximately 23 nm for the current experiment. Because the local deformation of the membrane under the tip does not change substantially as the probe tip moved across the membrane (Fig. 2F), the local strain field is fairly constant at all tip positions. The local deformation is also expected to be fairly independent of gate voltage since the cusp of the deformation is controlled largely by the van der Walls force from the probe tip (fig. S9) *(18)*.

Peak areal strains up to ≈1 % are predicted (Fig. 4A) in the graphene lattice directly under the tip. This strain produces pseudofields that could directly affect the graphene charge carriers *(3–11)*. The symmetry of the pseudofields is determined by the corresponding symmetry of the strain field. For example, a uniform pseudomagnetic field requires a special strain field *(4)* distorted with 3-fold symmetry. In our case, a rotationally symmetric strain field generates a 3-fold pseudomagnetic field with alternating signs *(6, 7)*. Figure 4B shows the calculated pseudomagnetic field for the strain field in Fig. 4A for the suspended membrane resulting in alternating spatial fields of ±10 T. The region where the pseudofield is maximal is ≈ 10 nm in diameter for the 50 nm membrane diameter used in the simulation. Using the same scaling as described above results in an effective pseudofield diameter of ≈45 nm *(18)*.

Carriers in graphene can penetrate large potential barriers due to the effect of Klein tunneling *(22)*, and physical barriers are typically engineered *(23)* to confine carriers. The pseudomagnetic field spatially confines the graphene carriers curving the classical trajectories and forming clockwise and counter-clockwise orbits around the alternating peaks of the pseudomagnetic field *(6, 7)*. However, some electronic states corresponding to classic snake

orbits that propagates along the lines where pseudomagnetic field changes sign will not be confined. We suggest that the application of external magnetic field suppresses such leaky orbits by canceling one component of the pseudomagnetic field that opposes the applied magnetic field, which improves the overall confinement as observed in Fig. 3, B-D. The dot size estimated from the charging energies in the gate maps (Fig. 3G) is about 34 to 53 nm in diameter, which is in reasonable agreement with the size of the estimated pseudofield (45 nm). The density of states peaks observed as the weakly negative sloping lines in the gate maps (Fig. 3A) may be caused by localization in a spatially varying pseudofield *(6, 7, 10)*, although a detailed model is currently not available. The variations in positive slopes bands (Figs. 3, B to D) are likely caused by minor deformations of the overall membrane shape affecting the size of the quantum dot.

Figure Captions

Figure 1: Scanning tunneling microscopy measurements of graphene drumheads. (**A**) Optical image of the gated graphene device. The device consists of a single graphene layer placed over an array of pits (1.1 μm in diameter, 100 nm in depth) etched in SiO_2 (300 nm)/Si substrate. (**B**) Magnified optical image of the device in (A). The single layer graphene region is marked by a red line. (**C**) Scanning electron microscope (SEM) image of the device. STM topographic images, 20 nm x 20 nm, on the supported graphene (**D**) and suspended graphene membrane (**E**). The insets show the graphene atomic lattice images, 5 nm x 5 nm. The inset grey scales cover the range of ±0.2 nm. (**F**) Topographic height histograms from the images in (D) and (E).

Figure 2: STM images and simulations of the deformed graphene membrane induced by competing forces of the STM probe tip and the back gate electric field. (**A**-**D**) STM topographic images of the graphene membrane for different gate voltages: 0 V (A), 20 V (B), 40 V (C) and 60 V (D). The membrane is deformed by upward forces from the STM tip and a downward force due to the electric field from the applied V_{GATE}. (**E**) Atomistic model showing deformations in the graphene membrane interacting with the STM tip. The radii of the tip and membrane in this model are 2.5 nm and 25 nm, respectively. (**F**) Calculated membrane shapes at the critical tip height for horizontal tip positions of 2.5 nm, 5.2 nm and 25 nm from the membrane edge. A back gate force of 0.012 pN was applied to the atoms in the membrane. The grey dashed curve is an envelope showing the membrane height as seen in an STM measurement.

Figure 3: Scanning tunneling spectroscopy of a suspended graphene membrane. (**A**) dI/dV gate map spectra on the suspended graphene membrane at B = 0 T. Each map is built of dI/dV vs. V_B spectra taken at multiple fixed V_{GATE}. The color scale is the dI/dV magnitude, which varies from 0.05 nS (dark) to 1.7 nS (bright) for (A) and to 1.2 nS (bright) for (B-D). The rectangle shows the region where individual spectra are obtained and plotted in (E). The blue arrows indicate spectral bands with positive slope that become more resolved at higher fields in (B-C). dI/dV gate map spectra on the suspended graphene membrane at (**B**) B = 5 T and (**C**) B = 8 T. The rectangle shows the region where individual spectra are obtained and plotted in (F). (**D**) dI/dV gate map spectra at B = 8 T, showing the variability in the measurements. (**E**) dI/dV vs. V_B spectra from the B = 0 T gate map in (A) for gate voltages varying from -1 V to 1 V. (**F**) dI/dV vs. V_B spectra from the B = 8 T gate map in (C) for gate voltages varying from 5 V to 6 V. The spectra are shifted vertically for clarity in (E) and (F). (**G**) The quantum dot addition energies corresponding to the difference in dI/dV peak positions in the spectra from the gate maps in (C) red symbols, and (D) blue symbols. Energies are converted from bias voltages using the lever arm, $E = \alpha V_B$, where $\alpha = 0.45 \pm 0.03$. The error bars in (G) are dominated by the statistical error in α, which was determined from one standard deviation uncertainties in the measured slopes of the charging lines in the gate maps. These uncertainties in turn determine the corresponding uncertainties in the capacitance ratios discussed in the main text.

Figure 4: Simulations of a graphene membrane shape and corresponding strain and pseudomagnetic field. (**A**) Graphene membrane shape with the STM tip positioned over the center of the membrane at zero back gate force. The inset shows a zoomed-in region where the strain is maximal. The radii of the tip and membrane in this model are 2.5 nm and 25 nm,

respectively. (**B**) The pseudomagnetic field, calculated from the strain in (A) (fig. S10) *(18)*, shows spatially alternating field with three-fold symmetry which can spatially confine carriers.

References

1. K. S. Novoselov et al., *Proc. Natl. Acad. Sci. USA* **102**, 10451–10453 (2005).

2. K. I. Bolotin et al., *Solid State Communications* **146**, 351–355 (2008).

3. M. M. Fogler, F. Guinea, M. I. Katsnelson, *Phys. Rev. Lett.* **101**, 226804 (2008).

4. F. Guinea, M. I. Katsnelson, A. K. Geim, *Nat Phys* **6**, 30–33 (2010).

5. N. Levy et al., *Science* **329**, 544 –547 (2010).

6. K.-J. Kim, Y. M. Blanter, K.-H. Ahn, *Phys. Rev. B* **84**, 081401 (2011).

7. G. M. M. Wakker, R. P. Tiwari, M. Blaauboer, *Phys. Rev. B* **84**, 195427 (2011).

8. F. Guinea, B. Horovitz, P. Le Doussal, *Phys. Rev. B* **77**, 205421 (2008).

9. F. Guinea, A. K. Geim, M. I. Katsnelson, K. S. Novoselov, *Phys. Rev. B* **81**, 035408 (2010).

10. T. O. Wehling, A. V. Balatsky, A. M. Tsvelik, M. I. Katsnelson, A. I. Lichtenstein, *EPL (Europhysics Letters)* **84**, 17003 (2008).

11. M. Gibertini, A. Tomadin, M. Polini, A. Fasolino, M. I. Katsnelson, *Phys. Rev. B* **81**, 125437 (2010).

12. S. Jung et al., *Nat Phys* **7**, 245–251 (2011).

13. A. Luican, G. Li, E. Y. Andrei, *Phys. Rev. B* **83**, 041405 (2011).

14. J. A. Stroscio, E. W. Hudson, S. R. Blankenship, R. J. Celotta, A. P. Fein, *Proceedings of SPIE* **4608**, 112–115 (2002).

15. G. M. Rutter et al., *Nat Phys* **7**, 649–655 (2011).

16. D. L. Miller et al., *Science* **324**, 924–927 (2009).

17. G. Li, A. Luican, E. Andrei, *Phys. Rev. Lett.* **102**, 176804 (2009).

18. Additional supplementary text and data is available in *Science* online.

19. B. J. LeRoy, J. Kong, V. K. Pahilwani, C. Dekker, S. G. Lemay, *Phys. Rev. B* **72**, 075413 (2005).

20. L. P. Kouwenhoven, D. G. Austing, S. Tarucha, *Reports on Progress in Physics* **64**, 701–736 (2001).

21. The one standard deviation error estimates in the quantum dot sizes were determined by combining the one standard deviation in the addition energy variation for the first and last set of energies in Fig. 3G, together with the one standard deviation uncertainties in the measured slopes of the charging lines in the gate maps.

22. M. I. Katsnelson, K. S. Novoselov, A. K. Geim, *Nat Phys* **2**, 620–625 (2006).

23. J. Güttinger et al., *Phys. Rev. Lett.* **103**, 046810 (2009).

24. Acknowledgements: We thank Mark Stiles and Shaffique Adam for valuable discussions, and Steve Blankenship and Alan Band for technical assistance. The U.S. National Science Foundation is gratefully acknowledged via grants CMMI-1069076 and CMMI-1129826 (TL and SZ) and grant CMMI-0841840 (CAW and SDS).

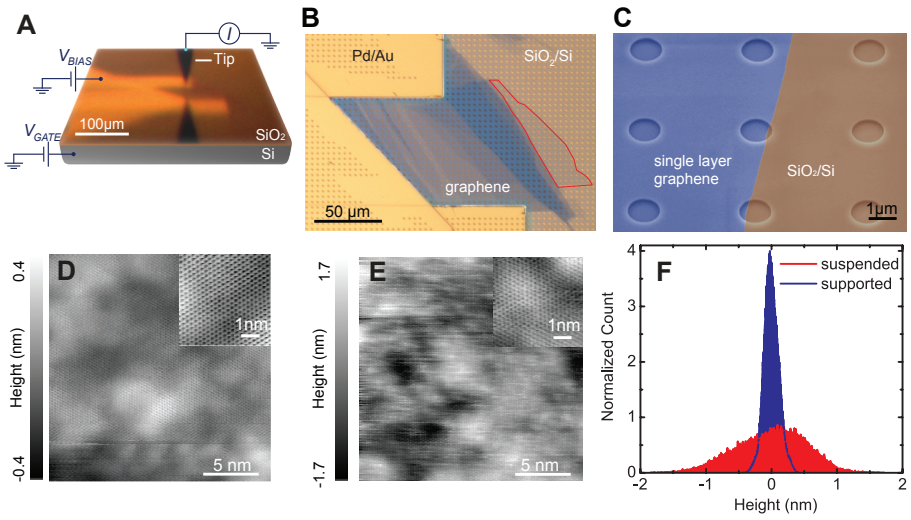

Klimov Fig.1, print full 2 columns 12 cm wide.

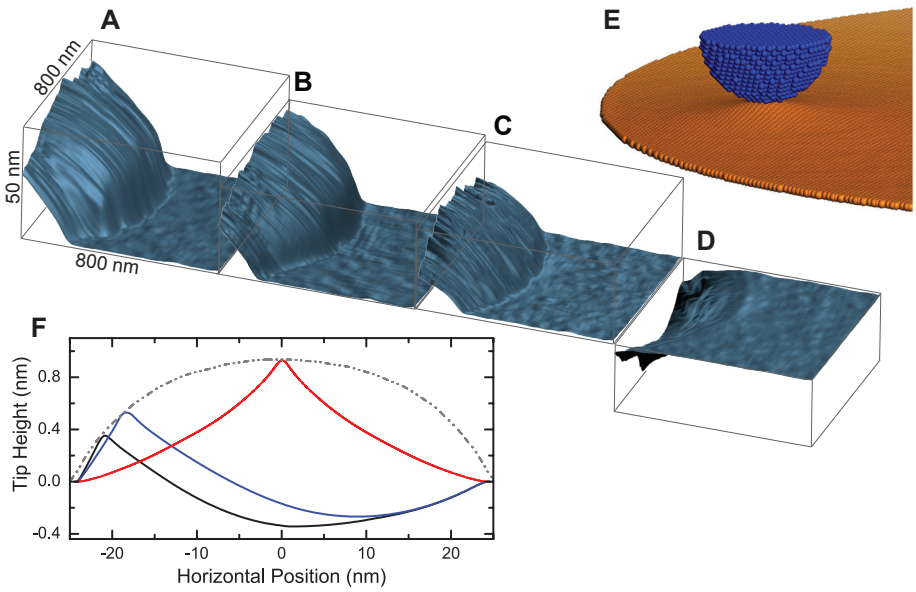

Klimov Fig. 2, print full 2 columns 12 cm wide.

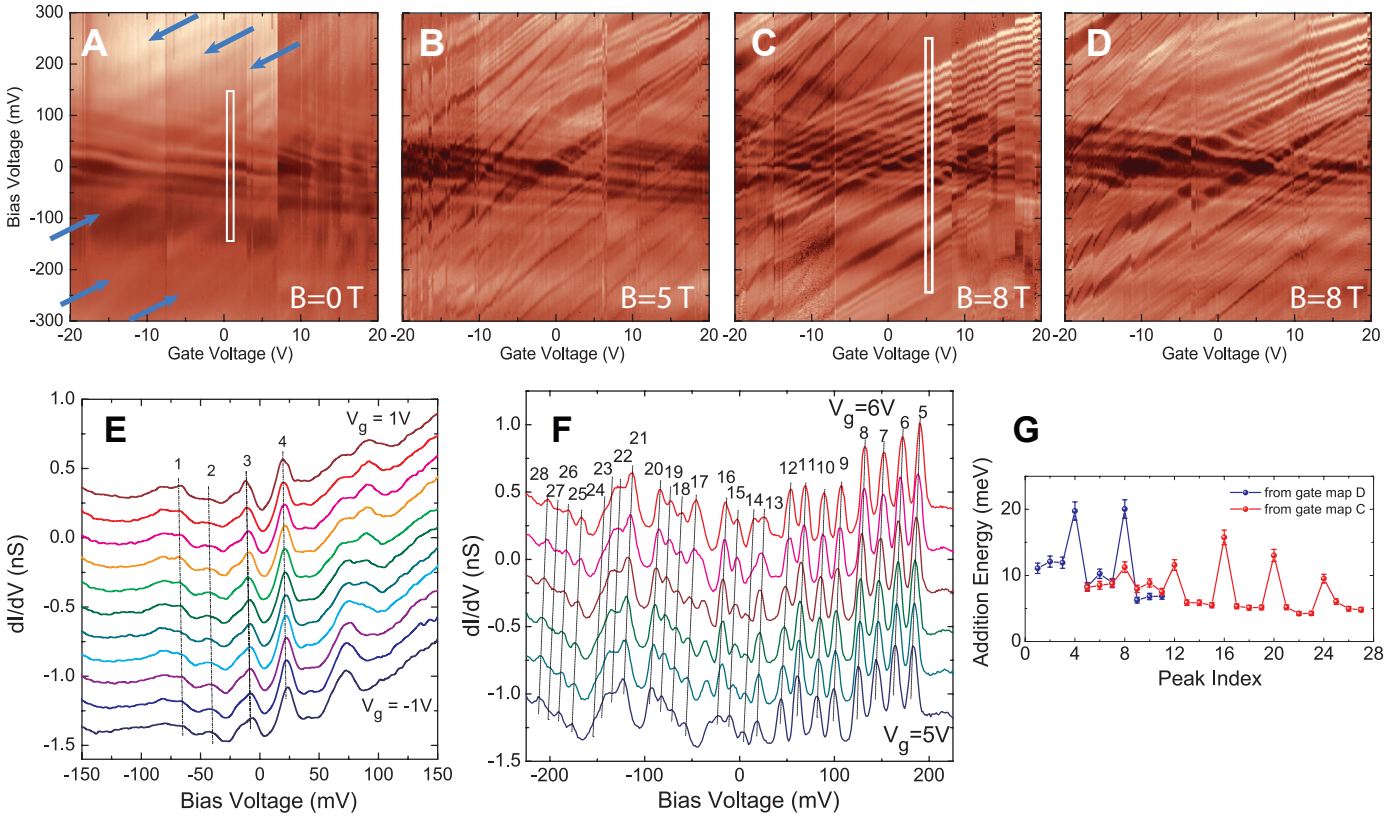

Klimov Fig. 3, print full 3 columns 18 cm wide.

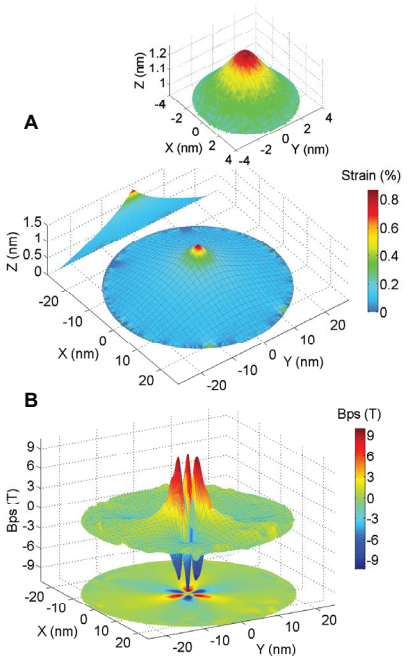

Klimov Fig. 4, print 1 full column 5.8 cm wide.